https://doi.org/10.2352/AIT.2026.1.1.6

Modelling the Wood-Graining Effect: A Coupled LES–Lagrangian–Film Framework for Next-Generation Printhead Design

Jason Leong and Vinh-Tan Nguyen, Institute of High Performance Computing (IHPC), Agency for Science, Technology and Research (A*STAR) (Singapore); Satoshi Watanabe, Seiko Future Creation Inc. (Japan); and Toshimitsu Morooka, SII Printek Inc. (Japan).

Abstract

The wood-graining effect is a print defect arising from complex aerodynamic interactions within the narrow gap between printhead and substrate. Unsteady vortical structures, substrate-induced Couette flows and drop-induced entrainment destabilise jetting trajectories, leading to wavering and consolidation of printed tracks. Conventional Reynolds-Averaged Navier–Stokes (RANS) turbulence models fail to capture these transient dynamics, necessitating high-fidelity turbulence modelling. In this study, large eddy and detached eddy scale resolving turbulence model driven computation fluid dynamics (CFD) simulations are combined with a two-way Lagrangian particle tracking framework to resolve the mutual interactions between jetted droplets and surrounding gas flows. This coupling accounts for shielding, wake effects, and drop-induced airflow modifications that drive cross-stream displacement. To connect droplet flight dynamics with final print quality, a surface film model simulates spreading, coalescence and redistribution upon impact on the substrate, directly linking flow-driven instabilities to visible wood-graining artifacts. The resulting CFD–Lagrangian–film framework provides a predictive description of wood-graining under realistic conditions, enabling systematic exploration of nozzle pitch, print gap and substrate speed. Demonstrated in 600 npi printheads, the study highlights how high nozzle density magnifies the impact of small aerodynamic disturbances. By establishing a physics-based understanding of wood-graining onset and evolution, the methodology supports the design of next-generation printheads and airflow control strategies to mitigate aerodynamic instabilities.

Introduction

Inkjet printing relies on the precise deposition of picoliter scale droplets across a substrate that often moves at high speed relative to the printhead. Maintaining accurate droplet placement is critical for industrial applications including high-resolution graphics, electronics, and functional coatings. However, print quality is frequently degraded by aerodynamic interactions that occur within the throw distance separating printhead and substrate.

Under certain operating conditions, these interactions with air flow induce lateral displacement of droplets, leading to the so-called wood-graining patterns, characterised by visible banding and striping, that limit achievable resolution and throughput (see Figs. 1 and 2). An example of wood-graining observed in a printed sample is shown in Fig. 2, where a characteristic horizontal modulation can be identified across the deposited surface.

Previous studies and reviews have identified strong coupling between ejected droplets and the unsteady airflow within the print gap, particularly for low-Stokes-number droplets (i.e., droplets with sufficiently small inertia to respond rapidly to the local airflow) [1]. Under conditions of high jetting frequency and dense nozzle arrays, interactions between droplet-induced flow and substrate-driven shear can lead to lateral displacement of droplets and the appearance of wood-graining.

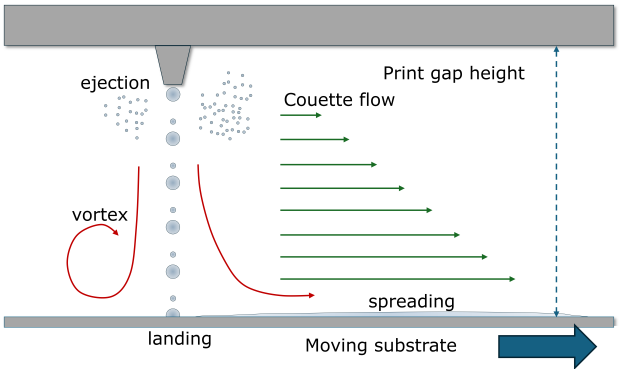

Figure 1. *Schematic illustration of aerodynamic interactions within the print gap height between the printhead and substrate. Substrate motion induces shear-driven Couette flow, while droplet ejection and wake recirculation generate unsteady vortical structures that drive lateral displacement prior to landing and spreading on the moving substrate.*

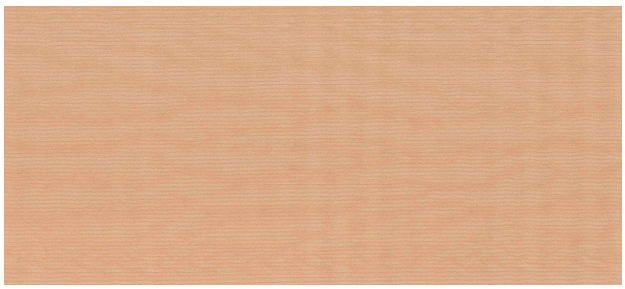

Figure 2. *Example of wood-graining observed in a printed sample (throw distance: 5 mm, jetting frequency: 15 kHz).*

Experimental investigations confirm the presence of shear-driven Couette flow arising from substrate motion, which forms a baseline airflow field within the print gap. Measurements using hot-wire anemometry and velocity profiling showed a nearly linear increase in streamwise air velocity between the printhead and moving web [2], consistent with a Couette flow type shear layer. Experimental visualisation and probe measurements further quantified the print gap airflow and similarly reported near-linear velocity distributions at modest substrate speeds [3]. These observations indicate that a significant substrate-driven shear flow exists even in the absence of strong droplet forcing, and that this baseline airflow interacts with droplet-induced disturbances

to modify droplet trajectories and contribute to aerodynamically driven print quality variations.

More recent work has shown that the flow field becomes increasingly complex when multiple nozzles operate in parallel [4]. Experimental visualisation demonstrated that reducing nozzle pitch increases the interaction between neighbouring droplet streams, leading to more pronounced recirculation and larger placement errors. High-speed imaging revealed the development of turbulent eddies and, under certain conditions, upstream of the droplet train, particularly for increased throw distances or low substrate speeds [4]. These findings suggest that the airflow cannot be characterised by single-nozzle operation alone, since much stronger disturbances emerge when larger numbers of nozzles fire simultaneously.

Despite these experimentally derived insights, the aerodynamics of multi-nozzle inkjet is not fully understood. Available literature focuses on flow visualisation and qualitative measurements, while quantitative characterisation of turbulence intensity, wake interaction and cross-stream displacement is limited. In particular, the near-substrate region is experimentally inaccessible to optical diagnostics, precisely where the highest vorticity gradients and flow instabilities are expected. Furthermore, while Couette-type shear flow has been well established, the unsteady turbulent vortices responsible for wood-graining have not been resolved in previous numerical studies. Conventional Reynolds-averaged Navier–Stokes (RANS) turbulence models tend to suppress the transient coherent structures that emerge at the nozzle scale and propagate downstream, thereby limiting their predictive capability.

Consequently, there is currently no numerical framework that captures the fully coupled interaction between unsteady air flow, droplet entrainment and surface impact. With industrial printheads increasingly adopting high nozzle densities often exceeding several hundred nozzles per inch, the aerodynamic sensitivity to small disturbances continues to grow, highlighting the need for high-fidelity modelling approaches capable of resolving these complex multiphysics interactions.

In this study, a scale-resolving large eddy and detached eddy simulation framework is developed and coupled two-way to a Lagrangian droplet model in order to resolve the unsteady aerodynamics responsible for wood-graining. A surface film model is incorporated to connect droplet flight dynamics with surface spreading and deposition, providing a fully integrated description of the wood-grain formation process. This combined CFD–Lagrangian–film approach enables systematic investigation of nozzle spacing, throw distance and substrate speed, and establishes a predictive, physics-based foundation for next-generation printhead design and aerodynamic control strategies.

Numerical Approach

The airflow in the print gap is resolved using high–fidelity turbulence modelling in order to capture the unsteady vortical structures associated with wood-graining. The computational framework combines large eddy and detached eddy simulation for the gas phase with a two-way coupled Lagrangian representation of ink droplets. A surface film model is further employed to describe the spreading and coalescence of droplets upon impact with the moving substrate. All simulations were performed using the open-source CFD platform `OpenFOAM` [5], which provides an extensible environment for Large Eddy Simulation (LES) or Detached Eddy Simulation (DES) turbulence modelling together with Lagrangian particle tracking and surface film capabilities.

LES Turbulence Flow Model

The airflow in the print gap is treated as an incompressible Newtonian fluid and is described by the filtered Navier–Stokes equations. An overbar denotes spatial filtering. The filtered continuity and momentum equations presented in index notation are:

$$\frac{\partial \bar{u}_i}{\partial x_i} = 0, \tag{1}$$

$$\frac{\partial \bar{u}_i}{\partial t} + \frac{\partial}{\partial x_j}\left(\bar{u}_i \bar{u}_j\right) = -\frac{1}{\rho}\frac{\partial \bar{p}}{\partial x_i} + \nu \frac{\partial^2 \bar{u}_i}{\partial x_j \partial x_j} + \frac{\partial \tau_{ij}^{SGS}}{\partial x_j} + \frac{1}{\rho} S_i^p. \tag{2}$$

Here $\bar{u}_i$ and $\bar{p}$ are the filtered velocity and pressure, ν is the kinematic viscosity, τ_{ij}^{SGS} denotes the deviatoric subgrid–scale (SGS) stress tensor, and S_i^p represents the momentum exchange source term with the Lagrangian droplets.

The SGS stress is defined as the deviatoric part of the residual stress arising from filtering and is modelled using an eddy–viscosity closure,

$$\tau_{ij}^{SGS} = -2\nu_t \bar{S}_{ij}, \tag{3}$$

where ν_t is the modelled turbulent viscosity and

$$\bar{S}_{ij} = \frac{1}{2}\left(\frac{\partial \bar{u}_i}{\partial x_j} + \frac{\partial \bar{u}_j}{\partial x_i}\right) \tag{4}$$

is the resolved strain–rate tensor. The isotropic part of the residual stress is absorbed into the modified filtered pressure.

LES resolves the energy-containing turbulent structures while modelling only the smallest subgrid scales, enabling prediction of unsteady turbulent vortices that is suppressed in conventional RANS approaches. In the present configuration, fully wall-resolved LES would in principle provide the highest fidelity, but remains prohibitively expensive for the wide range of print gap and nozzle-array configurations investigated here. A hybrid RANS–LES approach is therefore adopted as a computationally efficient alternative.

Most simulations employ a Detached Eddy Simulation (DES) formulation based on the Spalart–Allmaras (SA) RANS turbulence model [6] and its delayed-DES and improved-delayed-DES extensions (DDES and IDDES) [7, 8]. SA–IDDES automatically blends RANS behaviour in attached near-wall regions with LES behaviour in separated and unsteady flow, using a shielding function that prevents premature LES activation close to walls. This allows the dominant, unsteady structures in the print gap to be resolved at considerably lower cost than wall-resolved LES.

To provide higher fidelity in selected reference cases, wall-resolved LES is also employed using the Wall-Adapting Local Eddy-Viscosity (WALE) subgrid model [9]. WALE derives the eddy viscosity from invariants of the velocity-gradient tensor, accounting for both strain and rotation, and recovers the correct y^3 near-wall damping without dynamic procedures, enabling accurate representation of near-wall vorticity generation and transitional behaviour.

Taken together, the SA–IDDES and WALE closures provide scale-resolving simulations of the highly unsteady print gap aerodynamics, including the shear-driven Couette flow from the moving substrate and the jetting-induced vortices generated by successive droplet ejection from hundreds to thousands of nozzles.

Lagrangian Particle Modelling

Ink droplets are tracked as Lagrangian particles using the parcel-based formulation of the `OpenFOAM` Lagrangian library. Each parcel represents a number of droplets with identical properties. A point source description is adopted in which droplets are treated as spherical and sufficiently small compared with the resolved flow scales that deformation of the particles is neglected.

The particle kinematics are governed by the ordinary differential equations

$$\frac{\mathrm{d}x_{p,i}}{\mathrm{d}t} = u_{p,i}, \qquad m_p \frac{\mathrm{d}u_{p,i}}{\mathrm{d}t} = \sum F_i, \tag{5}$$

where $x_{p,i}$ and $u_{p,i}$ denote particle position and velocity respectively, m_p is the parcel mass, and the force sum includes drag, gravity/buoyancy and optionally pressure-gradient and lift contributions.

For the present configuration, the dominant contribution is aerodynamic drag. The drag coefficient C_D is evaluated using the standard `sphereDrag` formulation [10] in `OpenFOAM`, which combines two established particle-drag models [11, 12]. The particle drag force can then be described as,

$$F_{D,i} = C_D \frac{\pi D_p^2}{8} \rho \left(u_{f,i} - u_{p,i}\right) \left|u_{f,j} - u_{p,j}\right|, \tag{6}$$

where D_p is the particle diameter and ρ is air density. The air velocity $u_{f,i}$ is obtained from the resolved flow field interpolated to the particle position.

Gravity and buoyancy are combined as

$$F_{G,i} = m_p g_i \left(1 - \frac{\rho_f}{\rho_p}\right), \tag{7}$$

with ρ_p the particle density. Additional models such as pressure-gradient and lift forces are available, but only the dominant terms are activated in the present study.

Two-way momentum coupling is included by accumulating the equal-and-opposite force exerted by the parcels onto the air phase, allowing droplet-induced entrainment to influence the resolved gas flow. Particle–particle interaction (such as collisions or coalescence) is not considered, since only two-way coupling between droplets and air is applied in this study.

Surface Film Modelling

Droplets that reaches the substrate forms a thin surface film whose evolution is simulated using the surface film model in the `OpenFOAM` framework. The approach follows the lubrication–type formulation originally developed for partially wetted liquid films [13, 14], where the liquid layer is represented on a dedicated two–dimensional surface mesh coincident with the top surface of the solid boundary representing the substrate and is coupled to both the air and the Lagrangian particle field.

The depth–averaged mass continuity equation is

$$-\frac{\partial \rho \delta}{\partial t} + \nabla_s \cdot (\rho \delta U) = S_{\rho\delta}, \tag{8}$$

where ρ is the liquid density, δ the film thickness, U the mean film velocity, and $S_{\rho\delta}$ represents the net mass source due to impingement, splashing, evaporation, absorption into the substrate and film separation.

The corresponding momentum equation is

$$-\frac{\partial \rho \delta U}{\partial t} + \nabla_s \cdot (\rho \delta U U) = -\delta \nabla_s p + S_{\rho\delta U}, \tag{9}$$

where p is the effective pressure acting across the film and $S_{\rho\delta U}$ contains stress contributions tangential to the substrate. The pressure term includes components such as impingement pressure, splashing pressure, capillary and hydrostatic pressures, and local air phase pressure, while the stress term accounts for shear at the gas and wall interfaces, surface–tension and contact–angle forces, gravitational body force, and wall–tangential momentum transfer due to impingement, splashing and separation.

Each source contribution to the mass and momentum balances is implemented modularly. In the present study, only droplet–impingement sources and wall–tangential momentum transfer are activated, enabling the film to form and spread following impingement under isothermal conditions. Processes such as splashing, evaporation, boiling, and absorption into the substrate are available within the implemented model, but are not considered here. The surface film model is therefore used primarily to determine the impingement locations and spreading behaviour of droplets affected by aerodynamic effects, providing a link between the unsteady print gap air flow and the resulting wood-graining patterns on the print substrate.

High–Fidelity Simulation of Wood–Graining in Inkjet Printing

Previous studies of surface–mounted bluff bodies with varying wall proximity [15] demonstrated that near–wall separation, shear–layer development and recirculation beneath the body are strongly affected by the gap height. Those investigations examined several gap–to–length ratios and showed that wall proximity alters flow separation and reattachment beneath the body and modifies key features of the downstream wake. These results provide useful guidance for the present study, in which the print gap is treated as a parameter that affects the interaction between the shear flow and the jetted droplets. In the present work, a representative industrial print gap of $H = 5\,\mathrm{mm}$ is used in the baseline cases, while other practical values may also be considered.

Geometry and Computational Domain

Two reference configurations are investigated. In the SA–IDDES simulations, the substrate is treated as the moving component while the printhead remains stationary. In the wall–resolved LES cases, the inverse representation is used in which the printhead moves relative to a stationary substrate. In both formulations the computational mesh remains fixed and the relative motion is introduced through boundary conditions where the stationary object and the inlet are assigned the negative of the imposed motion, thereby ensuring that the same relative kinematics are obtained without employing a moving reference frame or mesh deformation.

The computational domain reproduces a representative section of a single printhead working in isolation above the moving substrate. Following the guidelines of [15], the domain dimensions are chosen such that the overall blockage ratio remains below 3%, ensuring that the imposed boundary conditions do not artificially confine the shear layer and separated structures in the print gap. A uniform inflow condition is applied at the inlet and a zero–gradient condition at the outlet, while slip boundary conditions are used on the lateral sides to minimise side–wall confinement. No–slip conditions with appropriate wall functions are prescribed at the printhead and substrate. The mesh is generated in `Gmsh` [16, 17] and imported into `OpenFOAM`. Fig. 3 illustrates the geometry and boundary specification for the LES configuration, in which the printhead motion is prescribed as a moving boundary.

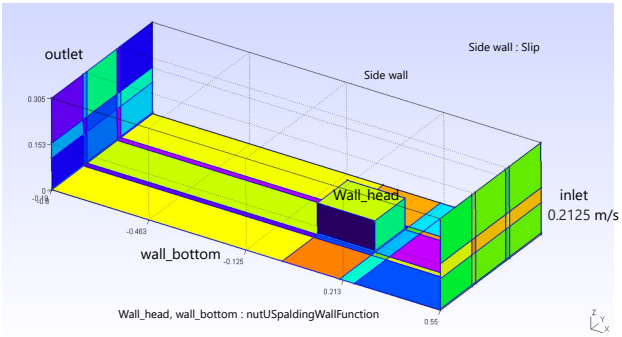

Figure 3. *Computational domain showing the printhead surface (wall_head), substrate (wall_bottom), and inflow/outflow boundaries. A moving–wall condition is applied at the substrate, slip is used at the lateral sides, and outlet is treated as zero–gradient. The mesh is generated using* Gmsh*.*

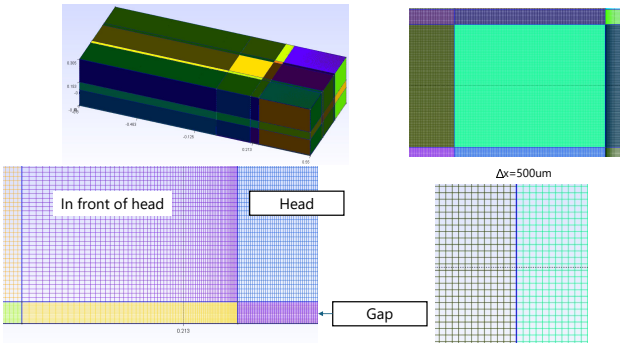

Figure 4. *Structured hexahedral mesh generated in* Gmsh *for the LES test case. The mesh contains approximately* 255 *million cells with a characteristic grid spacing of* $\Delta \approx 500\,\mu\mathrm{m}$ *in the bulk region and refinement within the* 5 mm *print gap.*

Mesh Design and Resolution Criteria

A hexahedral mesh is employed and refined in the gap region to capture the unsteady turbulent vortices associated with droplet entrainment. The first cell height on both the substrate and the printhead is selected based on near wall resolution criteria used for hybrid RANS–LES of wall-mounted obstacles. In particular, $y_1^+ \lesssim 1.5$ was adopted as a reference following the guidance in [15], with most cells in the gap having $y^+ < 1$.

In the SA–IDDES configurations, several mesh variants were assessed with total cell counts between approximately 2–5 million and near wall resolutions ranging from $y^+ \approx 0.75$ to $y^+ \approx 15$. The resulting flow fields showed only minor differences in the mean gap flow and in the dominant recirculating structures, indicating that SA–IDDES can remain robust even when the first grid point lies within the buffer region or the lower logarithmic layer. These cost-effective IDDES meshes therefore served as a test bed for evaluating nozzle array placement, operating conditions and boundary settings prior to the more expensive LES cases.

For the wall-resolved LES simulations, the mesh was refined such that $y^+ \lesssim 4$ along both the printhead and the substrate, placing the first grid points within the viscous sublayer (see Fig. 4). The resulting LES meshes contain approximately 255 million hexahedral cells with characteristic spacing $\Delta \approx 500\,\mu\mathrm{m}$ in the bulk region and strong refinement inside the 5 mm print gap, as illustrated in Fig. 4. This level of resolution is required to resolve the smaller turbulent structures and droplet-induced vortices that govern the onset of wood-graining.

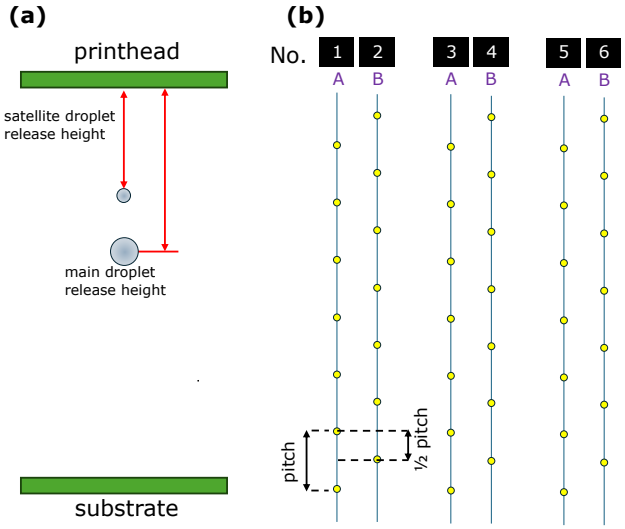

Figure 5. *(a) Injection model for each nozzle, releasing a main and satellite droplet per jetting event with prescribed initial velocity, volume, and elevation above the substrate. (b) Staggered nozzle layout (three rows,* 1920 *injectors) used as Lagrangian injection sites the simulations.*

Operating Conditions and Boundary Conditions

The airflow is treated as incompressible at low Mach number, with a uniform inlet velocity and ambient pressure at the outlet. No-slip boundary conditions are assigned on the solid surfaces, while lateral boundaries use slip conditions. The relative motion between printhead and substrate is imposed using the boundary–condition approach described in the Geometry and Computational Domain subsection.

Droplet ejection is imposed by a set of Lagrangian injectors representing a single printhead. In total, 1920 injectors are defined, arranged in three staggered rows of 640 nozzles each (Fig. 5). Each injector introduces a primary and satellite droplet pair at every jetting event that consists a main droplet 6.0 pL and a satellite droplet of 1.0 pL. The main and satellite droplets are released at different positions within the print gap and with distinct injection velocities. A uniform jetting frequency of 5 kHz is prescribed for all nozzles, matching a head speed of $0.2125\,\mathrm{m/s}$.

Staged LES/DES Simulation Protocol

The simulation procedure follows a staged approach based on established hybrid RANS–LES practice for separated flows [15]. The aim is to ensure physically correct turbulence development in the print gap, and minimise computational expense prior to activating droplet and film physics.

Stage 1: Steady RANS initialisation. A steady SA-RANS solution is computed to establish a converged mean flow including Couette shear induced by the moving substrate/printhead. This avoids starting the LES/DES stage from a quiescent state and shortens the subsequent flow development period.

Stage 2: Unsteady SA–IDDES or WALE–LES. The turbulence model is then switched to the unsteady SA–IDDES or WALE–LES and the simulation is performed without the Lagrangian or surface film models until the unsteady flow attains a statistically steady state. A dimensionless time interval of $t^\star = tU_\infty/H$ is allowed for effects of the steady RANS initialisation to decay. This procedure follows common practice in hybrid RANS–LES simulations of separated flows and is analogous to the start–up approach adopted in [15].

Stage 3: Droplet and film model activation. After the unsteady flow is fully developed, Lagrangian particle model and

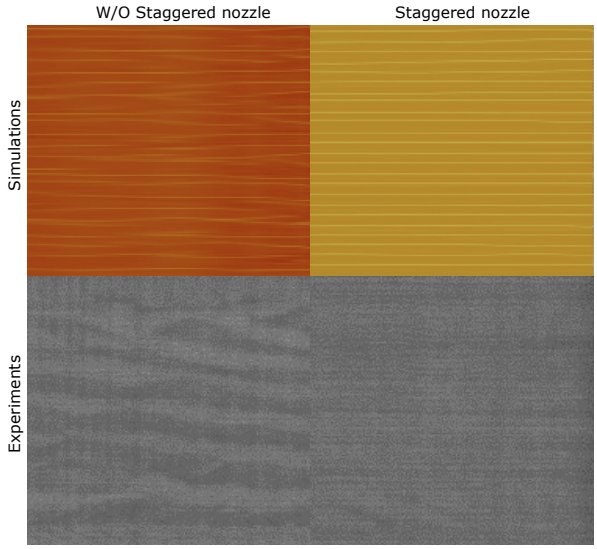

Figure 6. *Simulated surface film thickness fields (top) and corresponding physical print samples (bottom) for staggered (right) and non–staggered (left) nozzle configurations. The staggered layout weakens coherent aerodynamic deflection and reduces the visible wood–grain signature.*

Figure 7. *Left–to–right (L2R) lightness variation [18] measured on experimental print samples. Lower values correspond to reduced wood–graining. The staggered nozzle configuration exhibits consistently lower L2R than the non–staggered design.*

surface film modelling are activated. Unsteady statistics, droplet trajectories, and surface deposition patterns are collected over an averaging window sufficient to capture the dominant flow structures and droplet–induced entrainment.

This staged approach follows the simulation workflow, where the solution transitions from RANS to LES/DES and finally to the coupled flow–Lagrangian–film system. The procedure ensures that droplet deflection and surface spreading are evaluated under fully developed unsteady aerodynamics.

Effect of Nozzle Staggering on Wood–Graining

To examine whether nozzle layout influences the severity of wood–graining, both staggered and non–staggered nozzle arrangements with the same jetting frequency and droplet volumes are tested. In both cases the fully developed LES/DES aerodynamics obtained from the staged procedure were used, and Lagrangian droplets were released from 1920 injectors arranged in three rows, each injector releasing a main (6.0 pL) and a satellite (1.0 pL) droplet with a prescribed jetting velocity.

Fig. 6 compares the resulting surface film thickness fields and the corresponding experimental printouts. In the non-staggered configuration, periodic nozzle spacing produces a more coherent aerodynamic deflection pattern across the print gap, leading to visibly stronger lateral instabilities of deposited ink and hence a more pronounced wood–grain texture on the substrate. Introducing a half–pitch stagger between rows disrupts this periodicity and weakens the spatial coherence of the vortical structures interacting with the droplets. As a consequence, the lateral variation of deposited ink is reduced and the grain pattern becomes less visually perceptible.

The spatial modulation can be quantified using the “left–to–right” (L2R) lightness variation [18], in which the lightness field is collapsed into a one–dimensional profile and approximated by a polynomial fit. The maximum slope of this fitted profile serves as a scalar measure of low–frequency variation across the print. Applying this metric to both the simulated surface films and the experimental print samples shows consistently lower L2R values for the staggered layout compared with the non–staggered arrangement (Fig. 7), confirming that staggered nozzle placement is beneficial in mitigating wood–graining under otherwise identical operating conditions.

As further illustrated in the side–view velocity fields of Fig. 8, the non-staggered configuration generates pronounced periodic vortex structures upstream of each jet, whereas the staggered arrangement interrupts this periodicity and reduces coherent lateral forcing on the droplets.

Conclusion

High–fidelity simulations combining LES/DES turbulence models, Lagrangian particle tracking and surface film modelling have been developed to investigate the mechanisms governing wood-graining in inkjet printing. The staged workflow that involves steady RANS initialisation, unsteady LES/DES without droplets or surface film, and subsequent activation of particle and film models ensures that droplet impingement and ink spreading on the substrate occurs after the print gap flow field has fully developed.

The results confirm that instabilities of droplet trajectories is primarily driven by unsteady turbulent vortex structures inside the print gap, rather than by isolated nozzle behaviour. Introducing staggered nozzle arrangements disrupts the spatial coherence of these structures and reduces the severity of wood-graining effects. Simulated surface film patterns and experimental print samples show consistent L2R behaviour, demonstrating that the model captures the essential aerodynamic mechanisms responsible for wood-grain formation.

Beyond physical insight, the integrated LES/DES–particle–film framework provides a practical design tool, enabling different nozzle layouts and operating conditions to be evaluated a priori without expensive prototyping. The approach therefore offers a scientifically grounded alternative to optimise printhead arrangement, gap height and operating parameters before committing to experimental production.

Wall-resolved LES provides the highest fidelity but remains computationally demanding, particularly for realistic printhead geometries and industrially relevant Reynolds numbers. Future work will focus on accelerating the simulations through GPU-based solvers and hardware-specific optimisation, as well as investigating alternative turbulence-resolving approaches with reduced cost. The present methodology also accommodates additional physics such as evaporation, thermal coupling and substrate absorption, which will be incorporated as part of a broader plan to predict print quality under a wider range of industrial conditions.

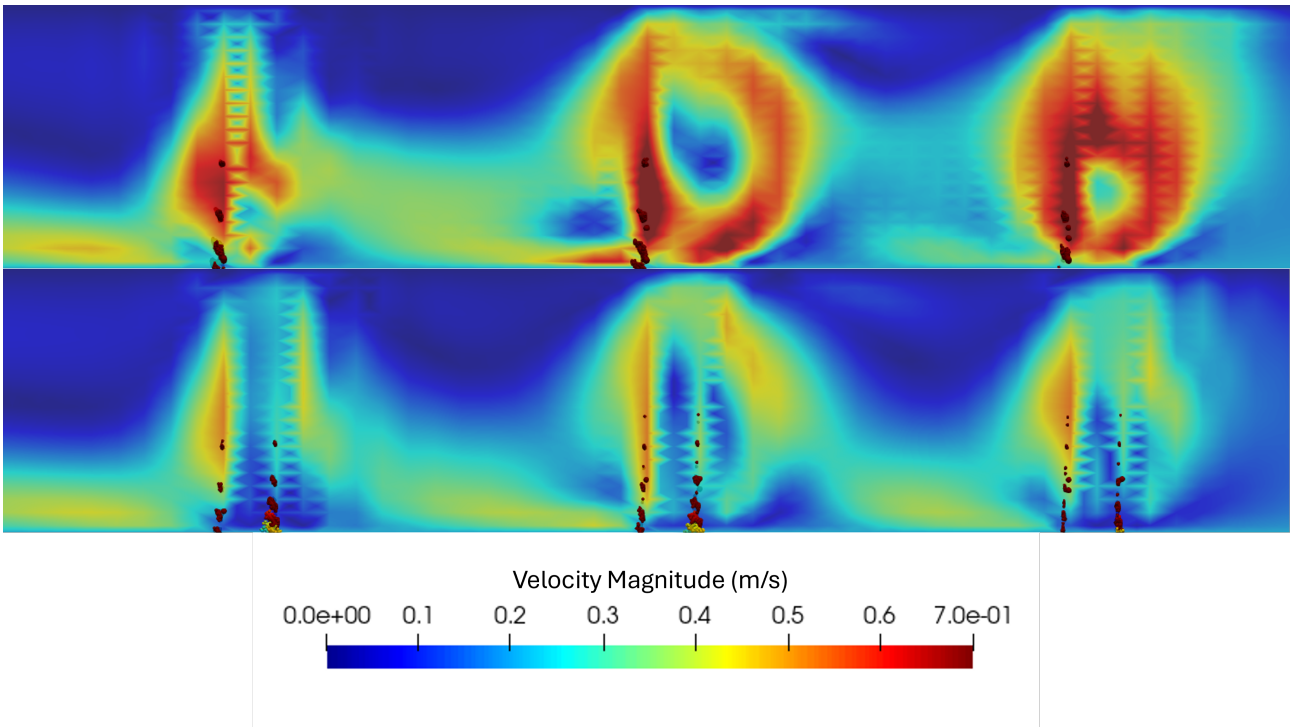

Figure 8. *Instantaneous side–view velocity magnitude (colour) overlaid with droplet parcels for non–staggered (top) and staggered (bottom) nozzle arrangements. Air flows from right to left. The non–staggered nozzle printhead case produces stronger periodic vortex structures upstream of each jet, which promote coherent lateral deflection of droplets, whereas staggering disrupts this periodicity and weakens the large–scale vortex motion.*

Acknowledgments

This research was conducted using the Wisteria/BDEC-01 and Oakbridge-CX Supercomputer Systems under the corporate usage program of The Information Technology Center, The University of Tokyo.

References

[1] Stephen D. Hoath. Wood-graining effects in inkjet printing. In Werner Zapka, editor, *Inkjet Printing in Industry: Materials, Technologies, Systems, and Applications*, chapter 2, pages 19–43. Wiley-VCH, Weinheim, Germany, 2022.

[2] N. Link, S. Lampert, R. Gurka, A. Liberzon, G. Hetsroni, and R. Semiat. Ink drop motion in wide-format printers: Ii. airflow investigation. *Chemical Engineering and Processing: Process Intensification*, 48(1):84–91, 2009.

[3] Wen-Kai Hsiao, Stephen D Hoath, Graham D Martin, and Ian M Hutchings. Aerodynamic effects in ink-jet printing on a moving web. *NIP28: 28TH International Conference on Digital Printing Technologies / Digital Fabrication 2012*, 28(1):412–415, January 2012.

[4] Cristina Rodriguez-Rivero, José Rafael Castrejón-Pita, and Ian M. Hutchings. Aerodynamic effects in industrial inkjet printing. *Journal of Imaging Science and Technology*, 59(4):040401–1–040401–10, July 2015.

[5] OpenFOAM home page. https://www.openfoam.org/, 2019.

[6] Philippe R. Spalart and Steven R. Allmaras. A one-equation turbulence model for aerodynamic flows. In *30th Aerospace Sciences Meeting and Exhibit*. American Institute of Aeronautics and Astronautics, January 1992.

[7] P. R. Spalart, S. Deck, M. L. Shur, K. D. Squires, M. Kh. Strelets, and A. Travin. A new version of detached-eddy simulation, resistant to ambiguous grid densities. *Theoretical and Computational Fluid Dynamics*, 20(3):181–195, Jul 2006.

[8] Mikhail L. Shur, Philippe R. Spalart, Mikhail Kh. Strelets, and Andrey K. Travin. A hybrid rans-les approach with delayed-des and wall-modelled les capabilities. *International Journal of Heat and Fluid Flow*, 29(6):1638–1649, 2008.

[9] F. Nicoud and F. Ducros. Subgrid-scale stress modelling based on the square of the velocity gradient tensor. *Flow, Turbulence and Combustion*, 62(3):183–200, September 1999.

[10] OpenCFD Ltd. OpenFOAM api documentation: `Foam::sphereDragForce`. https://www.openfoam.com/documentation/guides/latest/api/classFoam_1_1SphereDragForce.html, 2025. Accessed: 2025-12-01.

[11] A. Putnam. Integratable form of droplet drag coefficient. *ARS Journal*, 31:1467–1468, 1961.

[12] A. A. Amsden, P. J. O'Rourke, and T. D. Butler. Kiva-ii: A computer program for chemically reactive flows with sprays. Technical report, Los Alamos National Lab., NM (USA), 05 1989.

[13] K. V. Meredith, J. de Vries, and Y. Xin. A numerical model for partially-wetted flow of thin liquid films. In *Computational Methods in Multiphase Flow VI*, MPF11. WIT Press, June 2011.

[14] K. Meredith, Y. Xin, and J. de Vries. A numerical model for simulation of thin-film water transport over solid fuel surfaces. *Fire Safety Science*, 10:415–428, 2011.

[15] Yanan Wang, David Thompson, and Zhiwei Hu. Effect of wall proximity on the flow over a cube and the implications for the noise emitted. *Physics of Fluids*, 31(7):077101, 07 2019.

[16] C. Geuzaine and J.-F. Remacle. Gmsh: A three-dimensional finite element mesh generator with built-in pre- and post-processing facilities. *International Journal for Numerical Methods in Engineering*, 79(11):1309–1331, 2009.

[17] Gmsh website. https://gmsh.info/. Accessed: 2025-12-01.

[18] Ahmed H. Eid, Brian E. Cooper, and Edward E. Rippetoe. Characterization of mottle and low-frequency print defects. In Susan P. Farnand and Frans Gaykema, editors, *Image Quality and System Performance V*, volume 6808, page 680809. International Society for Optics and Photonics, SPIE, 2008.

Author Biography

*Jason Leong received his BE (2007) and PhD (2013) in Mechanical Engineering from Monash University, Malaysia. He is currently a researcher at A*STAR's Institute of High Performance Computing, Singapore, where his work focuses on computational fluid dynamics, mulciscale and multiphysics simulation, inkjet printing technologies, and urban microclimate modelling. He has contributed to research in fluid–structure interaction, dispersion modelling, and high-performance computing.*

*Nguyen Vinh-Tan received his BE (2002) in Aerospace Engineering from the Ho Chi Minh City University of Technology and PhD (2007) in Computational Engineering from the National University of Singapore in a joint programme with the Massachusetts Institute of Technology. He is currently a Senior Principal Scientist at the A*STAR's Institue of High Performance Computing, Singapore. His research focuses on developing computational methods for modelling and simulations of complex multiphysics engineering systems, with recent emphasis on translating advanced digital capabilities to support sustainable manufacturing, environment and energy applications.*

Satoshi Watanabe received his BS in Precision Mechanical Engineering (1996) and ME in Precision Engineering (1998) from Chuo University, Japan. He joined Seiko Instruments Inc. in 1998 and is currently with Seiko Future Creation Inc. He works on CAE across Seiko Group products, primarily focusing on inkjet printheads and watch development, as well as multiphysics problems involving piezoelectric, vibration, and fluid phenomena. He is a member of the Japan Society of Mechanical Engineers (JSME).

Toshimitsu Morooka received Bachelor's and Doctoral degrees in Engineering from Saitama University, Japan, in 1989 and 2004, respectively. In 1989, he joined Seiko Instruments Inc. and developed measurement devices based on superconductivity. In 2012, he joined SII Printek Inc., where he is engaged in the design of inkjet printheads using CAE.